Rapid and controllable synthesis of Fe_3O_4 octahedral nanocrystals embedded-reduced graphene oxide using microwave irradiation for high performance lithium-ion batteries

Rajesh Kumar [a, *], Rajesh K. Singh [b, **], Andrei V. Alaferdov [a], Stanislav A. Moshkalev [a]

[a] Centre for Semiconductor Components and Nanotechnology (CCS Nano), University of Campinas (UNICAMP), 13083-870, Campinas, Sao Paulo, Brazil
[b] School of Physical & Material Sciences, Central University of Himachal Pradesh (CUHP), Kangra, Dharamshala, H.P., 176215, India

ABSTRACT

We present a facile and simple method for the large-scale synthesis of octahedral iron oxide nanocrystals (Fe_3O_4 ONCs) on the reduced graphene oxide nanosheets (rGO NSs). The Fe_3O_4-ONCs embedded on the rGO NSs surfaces (Fe_3O_4-ONCs@rGO hybrids) are synthesized by microwave assisted. The Fe_3O_4 nanoparticles (Fe_3O_4 NPs) decorated rGO NSs (Fe_3O_4-NPs@rGO hybrids) are also synthesized using same method for comparative studies in lithium ion storage. During the synthesis process, rGO NSs served as the structural platform to embed the positively charged Fe_3O_4-ONCs on the basis of the electrostatic assembly followed by the microwave reduction of rGO NSs. Compared to Fe_3O_4-NPs@rGO, Fe_3O_4-ONCs@rGO hybrids shows superior electrochemical performance, including better cycling stability and rate performances, which may be attributed to the embedded structure of the nano-size Fe_3O_4-ONCs in rGO NSs. The electrochemical performances of the hybrids material as anode for lithium storage are evaluated by cyclic voltammetry and constant current charging and discharging. The synthesized Fe_3O_4-ONCs@rGO hybrids exhibited high lithium storage capacity, outstanding cycling stability (540 mAh g^{-1} after 120 cycles at 100 mA g^{-1}). This low-cost and fast synthesis strategy may be employed in other embedded structured hybrids design for high-performance lithium batteries.

© 2018 Elsevier Ltd. All rights reserved.

1. Introduction

In recent decades, high-power energy storage batteries have attracted immense attention because of the ever-growing markets of portable electronic devices and electric vehicles. The lithium-ion batteries (LIBs) have been widely applied as portable electronics and electric/hybrid devices due to its high energy density, high rate capability and environmentally friendly properties [1—4]. Also, LIBs are the highly utilized next-generation energy storage having higher energy density, good cycling lifetime, and lower self-discharge rate. The different anode materials used like transition metal oxides, metal sulfides, and silicon shows poor electron transport and slow Li-ion diffusion, which extensively increase the resistance at the electrolyte/electrode interface at high rate of charge/discharge [5—9]. So, it is quite an imperative matter to eradicate these problems and develop high-performance anode materials. Extensive research work has been done to improve ion and electron transport in electrodes to achieve high rate performance energy storage devices [10,11].

The metal oxides as anode materials in LIBs have attracted much attention due to their high theoretical capacities, eco-friendliness, natural abundance, low cost etc. [12—15]. But, bulk metal oxides normally exhibit poor cyclic life with low rate performance due to huge volume change during the charge/discharge process [16—18]. So, effective approach have been developed to address these issues by including carbonaceous materials with metal oxide (conductive and elastic carbon matrices, carbon nanotubes, graphite, conductive polymers etc.) which increases electron and ion transport and provides conducting support to metal oxide in the electrode materials [10,11,19—23]. However, large specific surface area with high electronic conducting carbon materials is needed for the well dispersion and distribution of metal oxide nanoparticle to avoid the agglomeration.

Graphene as two-dimensional carbon materials, containing

* Corresponding author.
** Corresponding author.
E-mail addresses: rajeshbhu1@gmail.com (R. Kumar), rksbhu@gmail.com (R.K. Singh).

large specific surface area and high electronic conductivity are considered as a high capacity storage materials as anode in LIBs. Monolayer or few-layer graphene can provide more active sites for lithium ion, not only on both sides of the carbon sheets but also on the edges and covalent sites of graphene fragments [24,25]. Thus, it is preferable to replace other carbonous materials using graphene for supporting metal oxides. Since graphene not only act as a volume buffer and electron conductor for metal oxides, but also suppress the aggregation of nanoparticles during cycles [26–28]. The high theoretical specific capacity (744 mAh g^{-1}) [24,29] and high chemical diffusivity for lithium ions (10^{-7}–10^{-6} cm^2 s^{-1}) [30,31] makes the graphene promising materials in the field of energy storage devices. Also, the volume or mass of graphene is so small compared to conventional electrodes made from carbonous material that it largely contributes to the total energy density of whole battery with higher space utilization. The derivatives of graphene such as graphene oxide (GO)/reduced graphene oxide (rGO) which can be obtained in large from chemical oxidation and reduction of graphite powder are frequently used in place of graphene in LIBs. The numerous studies on graphene/GO/rGO-metal oxide hybrids reveal enhanced energy storage capacity in LIBs [5,32–36]. The GO/rGO containing oxygen functional groups on its edges and basal surfaces helps in the attachment of metal oxide nanoparticles and play important role in LIBs [37]. Specific kind of structures and morphologies has been reported using various synthesis routes from ferrocene (Fe(C$_5$H$_5$)$_2$) with different constituents for the formation of Fe$_2$O$_3$/Fe$_3$O$_4$ nanostructures [38–40]. Wang et al. [38] synthesized using simple solvothermal method hierarchical branched hexapod of Fe$_3$O$_4$ for high specific saturation magnetization and large coercivity. Liu et al. [39] demonstrated low temperature synthesis and formation mechanism of carbon encapsulated spherical Fe$_7$S$_8$, equiaxed Fe$_3$O$_4$ and spherical porous FeOOH nanocrystals by electrophilic oxidation of Fe(C$_5$H$_5$)$_2$. Wang et al. [40] reported mesoporous Fe$_2$O$_3$ flakes (using Fe(C$_5$H$_5$)$_2$) encased within carbon skeleton, which demonstrate reversible capacity of 910 mAh g^{-1} (discharge/charge current of 0.1 A g^{-1}). As it is reported GO/rGO-Fe$_3$O$_4$ hybrids as anode exhibit improved cycling stability and high-rate performances [41–45]. While, most Fe$_3$O$_4$ NPs in GO/rGO-Fe$_3$O$_4$ hybrids are not well attached on surfaces and starts to move during the charge/discharge electrochemical performance and results in storage capacity degradation. Consequently, fabricating well attached Fe$_3$O$_4$ NPs on GO/rGO surfaces is one of the most effective strategies to improve the electrochemical performance.

In this article, we demonstrated a simple and fast approach for the large-scale (gram) synthesis of octahedral Fe$_3$O$_4$ nanocrystals embedded in the rGO NSs surfaces (denoted as Fe$_3$O$_4$-ONCs@rGO hybrids) from graphite oxide and Fe(C$_5$H$_5$)$_2$ by simple microwave-assisted in-situ exfoliation and reduction [46,47]. The contact established between Fe$_3$O$_4$-ONCs and rGO NSs not only prevent the aggregation of Fe$_3$O$_4$ ONCs but also can provide an efficient medium for lithium ion and electron transport. It is expected that the defect generated on the surfaces of rGO NSs by sharp edges of Fe$_3$O$_4$-ONCs are beneficial for the electrolyte penetration deep inside the rGO NSs. More interestingly, the as-synthesized Fe$_3$O$_4$-ONCs@rGO hybrids provide the right combination of electrode properties for high-performance LIBs. As a consequence, a highly reversible capacity, good rate capability, and excellent cyclic stability were achieved with the material as anode for lithium storage.

2. Experimental details

2.1. Preparation of graphite oxide and rGO NSs

All the chemicals employed in this study were of analytical grade and used as received and further the samples were synthesized by a simple and efficient microwave-assisted method. Graphite oxide was synthesized by chemical oxidation of natural graphite powder, using the modified Staudenmaier's method [48]. Graphite powder (5 g) was continuously stirred with a mixture of H$_2$SO$_4$ (90 ml) and HNO$_3$ (45 ml) solution at room temperature [49]. The solution container was placed into an ice-water bath to ensure constant temperature and subsequently, KClO$_3$ (55 g) was slowly poured into the solution to avoid explosion due to exothermic reaction. This solution was kept for five days under continuous magnetic stirring at room temperature for better oxidation of the graphite powder. The as obtained GO product was washed with DI water and further 10% HCl solution was added to remove sulphate and other ion impurities. It was then again and again washed with DI water until a pH of 7 was reached. Afterward the graphite oxide powder was treated with microwave irradiation (900 W for 1 min) for exfoliation and reduction into rGO NSs [50–53]. These graphite oxide powders were used in the next step for the synthesis of hybrids materials.

2.2. Preparation of Fe$_3$O$_4$-NPs@rGO and Fe$_3$O$_4$-ONCs@rGO hybrids

The synthesized graphite oxide (2 g) powder was dispersed into 100 mL of C$_2$H$_5$OH with sonication for 20 min for complete dispersion into solution. After that separately, 0.2 g of Fe(C$_5$H$_5$)$_2$ (Aldrich, 99.98%) was added into this solution with stirring for 15 min at room temperature. After that, diluted ammonia (NH$_3$·H$_2$O) (0.2 M) solution (10 mL) was drop wise added into the mixture for 10 min. Then it was dried in open atmosphere in sun light for complete evaporation of ethanol. After that, this chemically modified dry powder was divided into two parts (collected into quartz cup) and irradiated for different irradiation time (t$_1$ = 1.25 and t$_2$ = 1.75 min) using domestic microwave oven (Consul-CMW30AB) at 700 W for the final formation of Fe$_3$O$_4$-NPs@rGO and Fe$_3$O$_4$-ONCs@rGO hybrids.

2.3. Characterizations

The crystalline phases of the as-prepared rGO NSs and Fe$_3$O$_4$-ONCs@rGO hybrids samples were determined using an X-ray diffractometer (XRD - D/MAX-2500/PC; Rigaku Co., Tokyo, Japan) over 2θ range 10–65°. The surface morphology and elemental analysis were investigated using scanning electron microscope (SEM - Dual Beam FIB/FEG model FEI Nova 200) equipped with energy dispersive X-ray spectroscopy (EDS). Raman measurements were carried out to determine the defects in the material using a spectrometer with a 473 nm laser (NT-MDT NTEGRA Spectra). X-ray photoelectron spectroscopy (XPS) measurements were performed using a SPECS system XR 50 X-ray source (Al Kα, 1486.6 eV) equipped Phoibos 150 hemispherical energy analyzer with MCD 9 detector. Thermogravimetric measurement were carried out with a SDT Q600 Thermo-gravimetric analyses (TGA) apparatus (TA Instruments, USA), and the samples were heated at a rate of 10 °C/min from room temperature to 750 °C at air flow (100 mL/min) atmosphere.

2.4. Electrode preparation and electrochemical measurement

The anode for coin cells was prepared by Fe$_3$O$_4$-ONCs@rGO hybrids (as active materials 80 wt %), acetylene black (as conductive agent 10 wt%), and polyvinylidene fluoride (PVDF as binder 10 wt%) were dissolved in N-methylpyrrolidone (NMP) to form a slurry. The slurry was then pressed onto a Cu foil and dried in a vacuum oven at 110 °C for 11 h. The electrodes were pressed and cut into discs. The coin cell was fabricated in an argon-filled glove box. Coin cells

(CR2032) were fabricated with the as prepared anode, lithium metal as counter electrode, Celgard 2400 as separator and 1 M LiPF6 (1 M) in an ethylene carbonate(EC)/dimethyl carbonate (DMC)/diethyl carbonate(DEC) (EC/DMC/DEC, 1:1:1 vol%) as the electrolyte. The mass loading of each hybrid materials (active materials) for each electrode was ~2 mg. The electrochemical performance of the fabricated cell was tested in a potential window of $0-3.0$ V (vs. Li^+/Li) by a battery testing system (LAND CT, 2001A).

3. Results and discussion

Fig. 1 shows the schematic synthesis of Fe_3O_4-NPs@rGO and Fe_3O_4-ONCs@rGO hybrids. At initial steps, after microwave irradiation, the decomposed Fe atoms from $Fe(C_5H_5)_2$ gets the natural oxidation and aggregation to grow and forms into Fe_3O_4 NPs on the surfaces of rGO NSs. For longer time irradiation, the Fe_3O_4 NPs converts into Fe_3O_4 ONCs. The rGO NSs acts as negatively charged due to the presence of oxygen containing function groups and Fe_3O_4 NPs get attached on its surfaces due to the interactions [54,55].

Fig. 2 shows the SEM images of pristine rGO NSs obtained by reduction and exfoliation of rGO using microwave approach. The rGO exhibit the highly porous structure containing open edges with wrinkles and folding on its surfaces. Also, it can be seen that rGO NSs were highly interconnected to each others to form a complete networked structure with hollow interior and cross-sectional SEM images of rGO NSs contains large numbers of sub-micrometer pores.

To better understand the formation of Fe_3O_4-NPs@rGO and Fe_3O_4-ONCs@rGO hybrids (by Fe_3O_4 NPs and Fe_3O_4 ONCs), the morphology of the resulting sample were examined. For lower time microwave irradiation ($t_1 = 1.25$ min), Fe_3O_4 NPs on the surfaces of rGO NSs were created resulting in the formation of Fe_3O_4-NPs@rGO hybrids (Fig. 3a and b). The simultaneous exfoliation of graphite
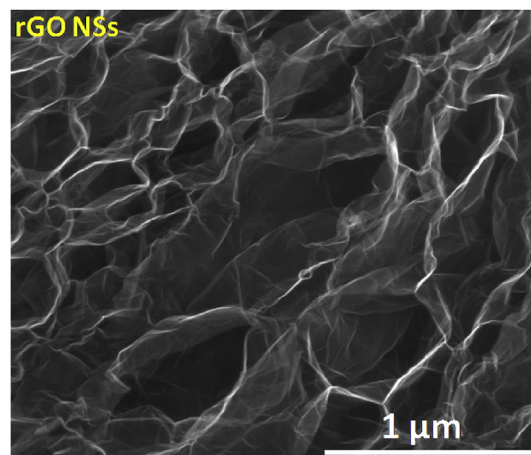

Fig. 2. SEM images of rGO NSs.

oxide into rGO NSs and decomposition of $Fe(C_6H_6)_2$ into Fe_3O_4 NPs finally produces the Fe_3O_4-NPs@rGO hybrids. The size of Fe_3O_4 NPs attached on the rGO NSs surfaces were ~50 nm and Fe_3O_4 NPs lie on the surfaces of rGO NSs.

When microwave irradiation was increased for longer time ($t_2 = 1.75$ min), these Fe_3O_4 NPs nucleate is some specified direction and produces octahedral like Fe_3O_4 NPs on the surfaces rGO NSs. Upon further extending the irradiation time, the amount of octahedral nanoparticles further increases accompanied with the shape becoming more regular as shown in Fig. 4. Fig. 4 shows a typical SEM image of the Fe_3O_4-ONCs@rGO hybrids in which most of the Fe_3O_4 ONCs were octahedral and uniformly distributed and attached on the surfaces of rGO NSs. Small amount of Fe_3O_4 NPs were still available in Fe_3O_4-ONCs@rGO hybrids, which do not
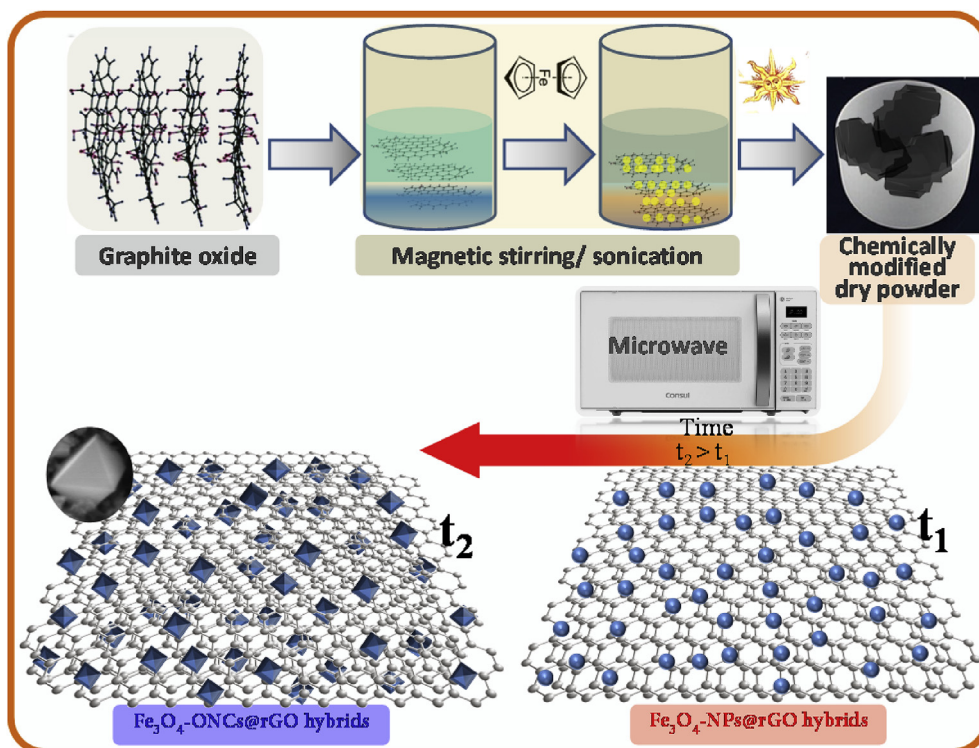

Fig. 1. Schematic illustration for the formation process of Fe_3O_4-NPs@rGO and Fe_3O_4-ONCs@rGO hybrids.
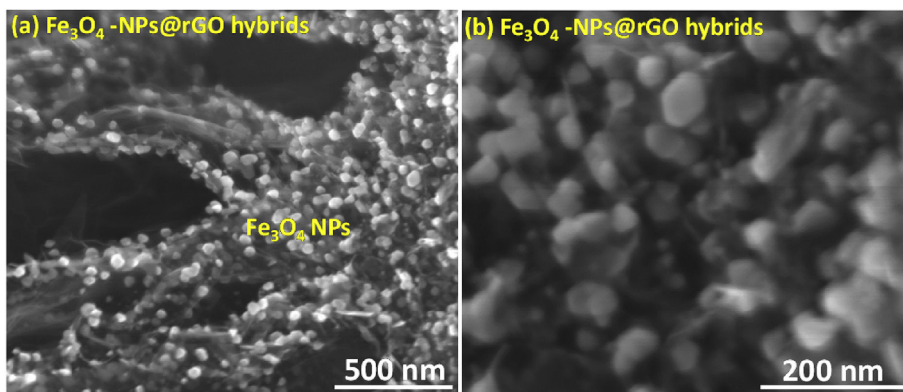
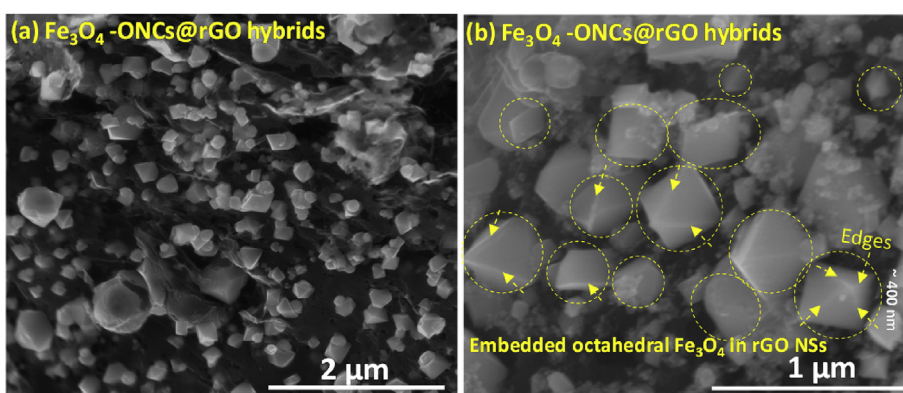Fig. 3. SEM images of Fe$_3$O$_4$-NPs@rGO hybrids.

Fig. 4. SEM images of Fe$_3$O$_4$-ONCs@rGO hybrids.

completely transform into Fe$_3$O$_4$ ONCs. From SEM images (Fig. 4), it can be clearly observed that the Fe$_3$O$_4$ ONCs (top view of Fe$_3$O$_4$ ONCs) are octahedral and it is expected that top surfaces of single Fe$_3$O$_4$ ONCs contains 6 vertices, 8 facets, 12 edges. These octahedral Fe$_3$O$_4$ ONCs have quite uniform structural dispersion with an average size of about ≤400 nm on the rGO surfaces. It was clearly found that the Fe$_3$O$_4$ ONCs were also partially encapsulated in rGO NSs. We have selected one intermediate microwave irradiation time (t' = 1.5 min; t$_1$<t'<t$_2$) to check the surface morphology and it was found that the synthesized hybrids contains combination of Fe$_3$O$_4$ NPs and Fe$_3$O$_4$ ONCs (Fig. S1). These specific selected microwave irradiation times (t$_1$, t', t$_2$) suggested that with increasing irradiation time, small sized Fe$_3$O$_4$ NPs transform into larger size Fe$_3$O$_4$ ONCs on the surfaces of rGO NSs.

The content of different element present in hybrids materials were determined by EDS analysis. Fig. 5a shows that the Fe$_3$O$_4$-ONCs@rGO hybrids mainly contain the C, O and Fe elements. Fig. 5b shows the XRD pattern of Fe$_3$O$_4$-NPs@rGO and Fe$_3$O$_4$-ONCs@rGO hybrids which were employed to determine the crystalline structure of synthesized materials. In Fig. 5b, the Fe$_3$O$_4$-ONCs@rGO hybrids exhibits a set of diffraction peaks with 2θ values around 30.1, 35.4, 43.1, 53.5, 57.0, and 62.6 correspond to lattice planes (220), (311), (400), (422), (511), and (400), respectively. The diffraction peaks suggest that the as-prepared Fe$_3$O$_4$-ONCs@rGO hybrid contains well crystallized Fe$_3$O$_4$ ONCs. These diffraction peaks confirms the face-centered cubic (fcc) inverse spinel structure of magnetite (JCPDS No. 65-3107) [56]. The XRD pattern of as synthesized Fe$_3$O$_4$-NPs@rGO hybrid represent variations in intensities with slightly change in angle position as compared to Fe$_3$O$_4$-ONCs@rGO hybrids.

In case of Fe$_3$O$_4$-NPs@rGO the higher intensity for Fe$_3$O$_4$ is at (400) whereas the growth direction is along (311) in Fe$_3$O$_4$-ONCs@rGO hybrids. The XRD peak in rGO NSs in the inset of Fig. 5b, appears at 2θ = ~26 correspond to 002 lattice plane of rGO NSs [49], and this peaks becomes narrow after the formation of Fe$_3$O$_4$-ONCs@rGO hybrids. These results indicate that the hybrids consist of rGO NSs and well crystallized Fe$_3$O$_4$ ONCs.

Fig. 5c shows the Raman spectrum of Fe$_3$O$_4$-NPs@rGO and Fe$_3$O$_4$-ONCs@rGO hybrids to confirm the defect after the formation of hybrids. The typical Raman spectrum of in Fe$_3$O$_4$-NPs@rGO and Fe$_3$O$_4$-ONCs@rGO hybrids shows two characteristic peaks of the D and G bands at ~1360 and ~1585 cm^{-1}, respectively. The peak intensity ratio of D-band to G-band (I$_D$/I$_G$) is related to the ratio of disordered sp^3 and ordered sp^2 carbon domains [57,58]. Fig. 5c, clearly shows that the ratio of I$_D$/I$_G$ increased after the formation of Fe$_3$O$_4$-NPs@rGO and Fe$_3$O$_4$-ONCs@rGO hybrids as compared to rGO NSs (inset). The calculated ratios of I$_D$/I$_G$ were 0.73, 0.86 and 0.98 for rGO NSs, Fe$_3$O$_4$-NPs@rGO and Fe$_3$O$_4$-ONCs@rGO hybrids, respectively. The increment of I$_D$/I$_G$ ratio for Fe$_3$O$_4$-NPs@rGO and Fe$_3$O$_4$-ONCs@rGO hybrids can be ascribed to the presence of defects due to the Fe$_3$O$_4$ NPs and octahedral Fe$_3$O$_4$ ONCs in rGO NSs.

The TGA measurements were used to find out the weight ratio of Fe$_3$O$_4$ ONCs in the synthesized Fe$_3$O$_4$-ONCs@rGO hybrids. The TGA under air has been used to determine the thermal stability of rGO NSs and Fe$_3$O$_4$-ONCs@rGO hybrids in the temperature range of 30–750 °C and the result is shown in Fig. 5d. It can be seen that the mass of rGO NSs vanishes (~96 wt%) and exhibits a three-step thermal decomposition starting from 30 °C to 750 °C [49]. The rGO NSs and Fe$_3$O$_4$-ONCs@rGO hybrids begins to lose weight up to
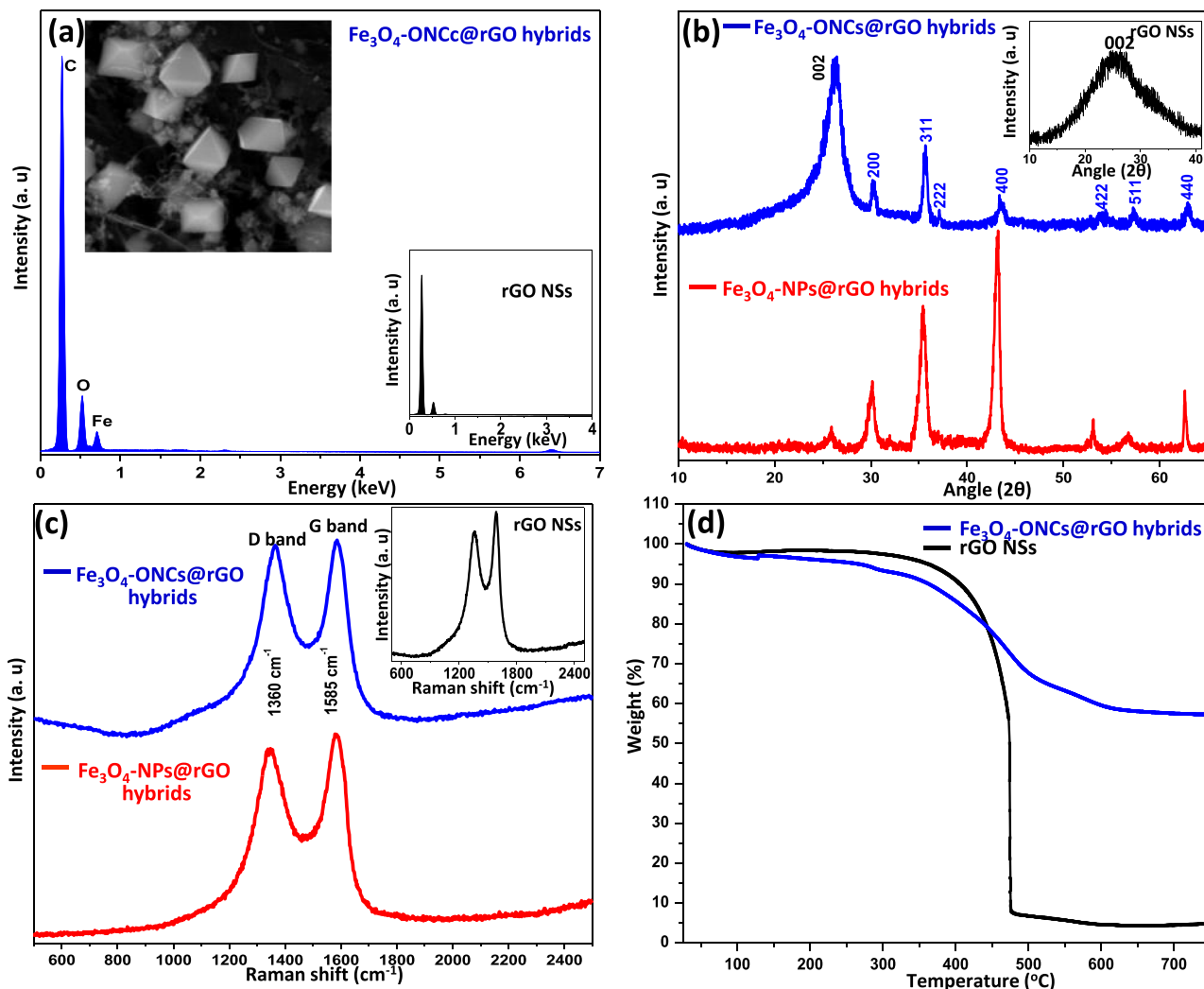
Fig. 5. EDS spectrum of Fe₃O₄-ONCs@rGO hybrids (b) XRD pattern of Fe₃O₄-NPs@rGO and Fe₃O₄-ONCs@rGO hybrids (inset: XRD of rGO NSs) (c) Raman spectra of Fe₃O₄-NPs@rGO and Fe₃O₄-ONCs@rGO hybrids (inset: Raman spectra of rGO NSs) and (d) TGA of rGO NSs and Fe₃O₄-ONCs@rGO hybrids.

3 wt% and 7%, respectively starting from 325 °C, attributed to the removal of adsorbed moisture and elimination of some residual oxygen-containing groups on its surfaces [59]. A very rapid and main decay in TGA curve for rGO NSs shows that a large weight loss (~90 wt%) is observed over the temperature range 325–475 °C and small loss (4 wt%) in the range of 475–750 °C. These weight losses in the higher temperature range (325–750 °C) is due to the decomposition of the labile oxygen-containing functional groups present in rGO NSs and combustion of rGO NSs skeleton in air [60,61]. The Fe₃O₄-ONCs@rGO hybrids shows that a sharp weight loss (~34 wt%) appeared from 325 to 610 °C and after reaching 750 °C, the Fe₃O₄-ONCs@rGO hybrids shows a total loss of ~43 wt%. Finally, at 750 °C we may have obtained Fe₃O₄ residue in hybrid as ~57 wt% (including remaining ~4 wt% rGO NSs) and this is mainly due to the decompositions of rGO NSs component from Fe₃O₄-ONCs@rGO hybrids.

The XPS analysis was performed to further evaluate the chemical composition of the synthesized hybrids materials. Fig. 6a shows the wide scan XPS spectrum of Fe₃O₄-ONCs@rGO hybrids. The peak at ~284, ~532, and ~711 eV consists of C, O and Fe elements, respectively. The atomic percentage (at%) of C, O and Fe were 78.19, 12.34 and 9.45, respectively. As shown in Fig. 6b, the deconvoluted peaks of C 1s spectrum of Fe₃O₄-ONCs@rGO hybrids can be fitted

with two component peaks at 284.5 and 286.5 eV, corresponding to C-C/C=C (284.6 eV) in the aromatic rings and C-O (286.5 eV) of epoxy groups, respectively [62,63]. In Fig. 6c, deconvoluted peak of O 1s spectrum shows two split peaks resulting from the different chemical bonding states of oxygen element in Fe₃O₄-ONCs@rGO hybrids. The peaks located at 530.2, 531.1, and 532.8 eV, which were attributed to oxygen in the lattice (Fe-O) [64], oxygen atoms in the surface hydroxyl groups (H-O), and oxygen in the lattice (C-O), respectively [63,65,66]. The Fe 2p XPS spectrum of the Fe₃O₄-ONCs@rGO hybrids exhibit two peaks at 711 and 722.5 eV corresponds to the Fe 2p$_{3/2}$ and Fe 2p$_{1/2}$ spin orbit peaks of Fe₃O₄ (Fig. 6d), confirming preparation of Fe₃O₄-ONCs@rGO hybrids [67]. The absence of the satellite peaks in the XPS also confirms that there is formation of Fe₃O₄ rather than Fe₂O₃ [66,68].

Cyclic voltammetry (CV) was performed to characterize the lithium ion dynamics of the hybrids materials. Fig. 7 shows the electrochemical properties of Fe₃O₄-NPs@rGO and Fe₃O₄-ONCs@rGO hybrid materials. Fig. 7a shows the 2nd cycle of CV curves in the voltage range of 0–3 V (vs Li/Li$^+$) at the scan rate of 10 mV s^{-1} for Fe₃O₄-NPs @rGO and Fe₃O₄-ONCs@rGO hybrids. The larger area of CV curve of Fe₃O₄-ONCs@rGO as compared to Fe₃O₄-NPss@rGO hybrids predicts the high storage capacity for Fe₃O₄-ONCs@rGO hybrids. Fig. 7a shows the obvious reduction and
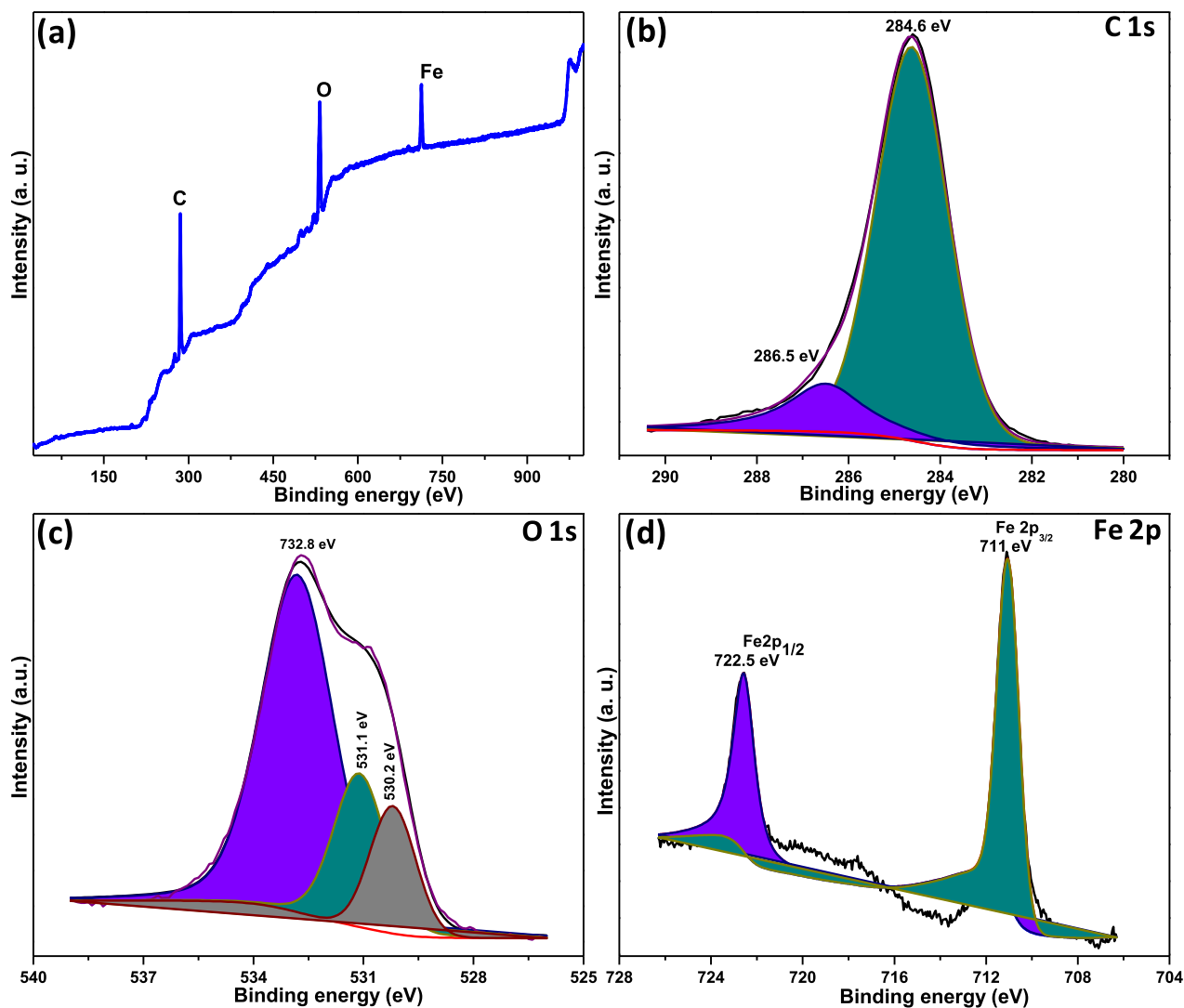
Fig. 6. (a) XPS survey scan of Fe₃O₄-ONCs@rGO hybrids, (b) C 1s, (b) O 1s, and (c) Fe 2p core-level XPS spectra of the Fe₃O₄-ONCs@rGO hybrids.

oxidation peaks. The CV profiles of the electrode in Fig. 7a shows the cathodic peaks at about 0.7–0.9 and anodic peaks at 1.6–1.7 V, corresponding to the electrochemical reduction/oxidation reactions ($Fe^{3+} \leftrightarrow Fe^0$) accompanying the insertion/extraction of lithium ions [69,70]. The CV curve clearly shows the slight variation in reduction voltage as 0.67 V and 0.88 V for Fe₃O₄-ONCs@rGO and Fe₃O₄-NPs@rGO hybrids, respectively. The slight change in reduction voltage shows the different reaction for these hybrids. The reduction peak around 0.67 V is found in the cathodic scan, which corresponds to the reduction of Fe₃O₄ (Fe^{2+}/Fe^{3+}) to Fe^0 and the formation of Li₂O via a conversion reaction as $Fe_3O_4 + 8Li^+ + 8e^- \rightarrow 3Fe + 4Li_2O$ [71,72]. In the anodic scan, there is a relatively weak anodic peak at ~1.62 V which attributes to the reversible oxidation of Fe^0 to Fe^{2+}/Fe^{3+} [73]. After second cycle, the CV curves of the Fe₃O₄-ONCs@rGO hybrids electrode were well overlapped, indicating good electrochemical reversibility due to the formation of the solid-electrolyte interface (SEI) layer [73,74].

Fig. 7b displays discharge profiles curve of the first cycle at 100 mAhg⁻¹ for Fe₃O₄-NPs @rGO and Fe₃O₄-ONCs@rGO hybrids. The discharge curves present a voltage plateau at ~0.8 V, which closely resembles to the reported literatures on Fe₃O₄ anode materials [75–78]. In both hybrids, the specific capacity of Fe₃O₄-

ONCs@rGO hybrid reaches ~1625 mAhg⁻¹, which is higher than that of Fe₃O₄-NPs@rGO hybrids (~1050 mAhg⁻¹). The result indicates that the morphological changes formed by Fe₃O₄ and rGO NSs (Fe₃O₄-NPs @rGO and Fe₃O₄-ONCs@rGO hybrids) bring out different electrochemical behaviors.

Long-term stability test reveals that the Fe₃O₄-ONCs@rGO hybrid exhibits excellent cycling stability. The excellent cycling performance and high reversible capacity of the Fe₃O₄-ONCs@rGO hybrids can definitely be attributed to the rGO modification. Fig. 7c shows the charge/discharge capacity for the synthesized hybrids at a current density of 100 mAg⁻¹ for 120 cycles. The curve clearly shows the decrease in the capacities of the Fe₃O₄-NPs@rGO hybrids for initial few cycles and after that it becomes nearly stable. From the 6th cycle onward, the Fe₃O₄-ONCs@rGO hybrids electrode exhibits a very stable capacity of 570 mA h g⁻¹ and still retains the capacity of 540 mA h g⁻¹ even after 120 cycles (only 0.04% capacity fading per cycle between cycles 7 and 120), while the capacity of the Fe₃O₄-NPs@rGO hybrids electrode gradually decreases to 285 mA h g⁻¹ at the 120th cycle. It indicates that the Fe₃O₄-ONCs@rGO hybrid shows better cycling stability as compared with the Fe₃O₄-NPs@rGO hybrids. This may be due to the embedded Fe₃O₄ ONCs in rGO NSs that enables the lithium ion transfer easier
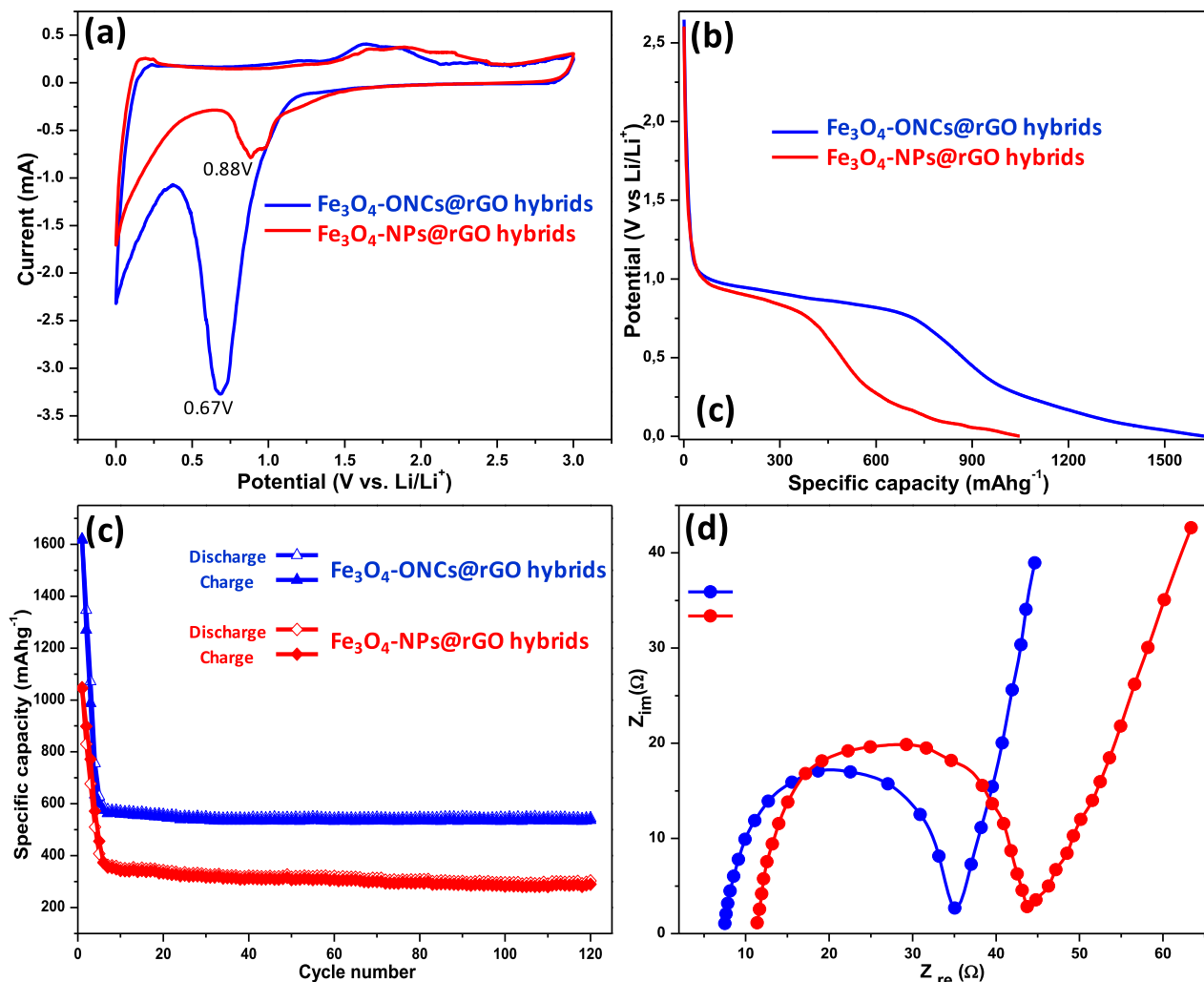
Fig. 7. Electrochemical properties of Fe$_3$O$_4$-NPs@rGO and Fe$_3$O$_4$-ONCs@rGO hybrids. (a) CV curves in a voltage range of 0.0–3.0 V (vs. Li/Li$^+$) at a scan rate of 10 mVs^{-1}, (b) the first discharge profiles at a current density of 100 mA g^{-1} (c) cycling performance of hybrids at current density of 100 mA g^{-1} for 120 cycles and (d) Nyquist plots over the frequency range from 0.1 MHz to 0.1 Hz.

inside rGO NSs layers during the charge/discharge process. Also, it is expected that the open structure of rGO NSs network (Fig. 2) provide an effective conducting network. More importantly, compared with the Fe$_3$O$_4$-NPs@rGO, the Fe$_3$O$_4$-ONCs@rGO hybrids could more effectively limit the volume expansion of Fe$_3$O$_4$ ONCs during the cycling process, resulting in the excellent cycling stability. Also, the defect produced by Fe$_3$O$_4$ ONCs were large as compared to Fe$_3$O$_4$ NPs on the surfaces of rGO NSs, this may also be a major reason for good performance of Fe$_3$O$_4$-ONCs@rGO as compared to Fe$_3$O$_4$-NPs@rGO hybrids. Table 1 represents the comparison and performance of Fe$_3$O$_4$-ONCs@rGO hybrids in this work with others reported works on Fe$_3$O$_4$-graphene/graphene nanosheets/rGO nanocomposite for LIBs.

The electrochemical impedance spectroscopy (EIS) was performed to experimentally probe lithium ion transfer resistance of these materials, as shown in Fig. 7d. At high applied frequencies region, the intercept of the real part of Z (Z$_{re}$) represents the ionic resistance of the electrolyte [92]. These resistances were nearly 11 and 7.5 Ω for Fe$_3$O$_4$-NPs@rGO and Fe$_3$O$_4$-ONCs@rGO hybrids, respectively. From the Nyquist plot, it can be found that the diameters of the semicircle for Fe$_3$O$_4$-ONCs@rGO hybrid electrodes were smaller than Fe$_3$O$_4$-NPs@rGO hybrids, which represent lower charge transfer resistance (R$_{ct}$) in Fe$_3$O$_4$-ONCs@rGO hybrids. The

diameters for semicircle were 34 and 25.5 Ω for Fe$_3$O$_4$-NPs@rGO and Fe$_3$O$_4$-ONCs@rGO hybrids, respectively. It means that Fe$_3$O$_4$-ONCs@rGO hybrids have the fast charge transfer behavior during the electrolyte performance. This result further suggests that Fe$_3$O$_4$-ONCs@rGO hybrid is favorable to the lithium transfer, while the Fe$_3$O$_4$-NPs@rGO is slightly resistive to the lithium ion transfer, resulting in the large charge transfer resistance.

4. Mechanism for the formation of Fe$_3$O$_4$-ONCs@rGO hybrids

During the synthesis of hybrids, the microwave temperature and irradiation time plays significant role in the formation of Fe$_3$O$_4$ morphologies. It is well known that the shape and morphology of crystals are generally controlled by the growth rates along special directions. Also, from the crystallographic point of view, the morphology of crystal is mostly controlled by the ratio of the growth rate along different directions. It has been proposed that a perfect octahedron structure can be formed when the ratio of growth rate along two direction are defined [93]. During the process of crystal growth, the reaction rate also affects the growth rate of different plane. When the temperature is raised at higher heating rate (10 °C/min) it results in nanoparticles having minimum surface energy. Octahedral nanoparticles have {111} planes as their flat facets, which

Table 1
Comparison on the structure and rate performance of Fe$_3$O$_4$-ONCs@rGO hybrids with other reported Fe$_3$O$_4$-graphene/graphene nanosheets/rGO nanocomposite for LIBs.

Synthesis methods	Nanocomposite/hybrids	Fe$_3$O$_4$ NPs/nanocrystal size (nm)	Current density (mA g^{-1})	Cycle number (Nth)	Retaining capacity (mAh g^{-1})	Ref.
Ultrasonic assisted co-precipitation	Fe$_3$O$_4$-graphene	10	4000	800	460	[79]
in-situ thermal reduction	Fe$_3$O$_4$-graphene	8–20	5000	1000	660	[80]
Thermal evaporation	Fe$_3$O$_4$-graphene	10–20	1000	200	539	[81]
Gas/liquid interface reaction	Fe$_3$O$_4$-graphene	12.5	1000	75	410	[82]
Hydrothermal	Fe$_3$O$_4$-graphene	3–15	100	100	650	[83]
Hydrothermal	Fe$_3$O$_4$-graphene	7	1600	25	474	[54]
in-situ hydrothermal	3D Fe$_3$O$_4$-graphene	5–6	92.5	50	605	[84]
Solvothermal	Fe$_3$O$_4$-graphene	<30	50	40	750	[85]
in-situ reduction	Fe$_3$O$_4$-graphene nanosheets	300	700	100	580	[75]
Gel-like film (GF) assisted solvothermal	Fe$_3$O$_4$ - graphene nanosheets	10	5000	700	324	[41]
Hydrothermal	Fe$_3$O$_4$-graphene nanosheets	5	1800	1200	437	[86]
Hydrothermal	Fe$_3$O$_4$-graphene nanosheets	10–20	50	50	675	[87]
Ultrasonic deposition	Fe$_3$O$_4$-graphene nanosheets	10–15	70	50	753	[88]
Ultrasonication and chemical reduction	Fe$_3$O$_4$-graphene nanoribbons	10	400	300	708	[89]
Hydrothermal	3D Fe$_3$O$_4$-GO	200	4800	50	363	[90]
High-temperature reduction	Fe$_3$O$_4$-rGO	<55	1850	80	200	[91]
Microwave	Fe$_3$O$_4$-ONCs@rGO	≤400	100	120	540	This work

possesses minimum surface energy and less surface defects [94]. In microwave heating, the temperature increases very fast during the irradiation on the samples. Also, in fcc crystal, a general sequence of surface energies hold, γ {111} < γ {100} < γ {110} [95] which means that the Fe$_3$O$_4$ crystals usually exist with {111} lattice planes as the basal surfaces and the {110} lattice planes with high surface energies are licked up during the growth of the Fe$_3$O$_4$ crystals [96]. Therefore, it can be expected that fabrication of Fe$_3$O$_4$ crystals possessing active basal surfaces ({110}) is significant for octahedral formation for Fe$_3$O$_4$. But, until now, the selective synthesis of uniform Fe$_3$O$_4$ polyhedral microcrystal with a well-defined shape has not been accomplished, to say nothing of Fe$_3$O$_4$ crystals with active surfaces ({110}) exposed to the surroundings [97].

5. Conclusions

In conclusion, we have developed a fast approach, simple method and single-step process for large scale synthesis of octahedral Fe$_3$O$_4$ NCs embedded on the surfaces of rGO NS (Fe$_3$O$_4$-ONCs@rGO hybrids) involving microwave-assisted synthesis. The rGO NSs provide the surface for embedding to Fe$_3$O$_4$ ONCs in the synthesized Fe$_3$O$_4$-ONCs@rGO hybrids. Compared to Fe$_3$O$_4$ NPs decorated rGO NSs (Fe$_3$O$_4$-NPs@rGO hybrids), the embedded-structured as Fe$_3$O$_4$-ONCs@rGO hybrids exhibits higher reversible capacity and better cycle/rate performance due to its unique structure. We are expecting that high lithium storage performance is mainly because of the unique structure of Fe$_3$O$_4$-ONCs@rGO hybrids which possesses synergistic effects to prevent aggregation, improve large volume change, and facilitate the transfer of electrons and electrolyte during electrochemical measurement. Benefiting from the synergetic effect of the Fe$_3$O$_4$ ONCs and rGO NSs, the hybrid exhibit high lithium storage capacity at 100 mA g^{-1}, high cycle stability (540 mAh g^{-1} after 120 cycles at 100 mA g^{-1}), and superior rate performance making it a very attractive anode material for LIBs. This study offers an alternative strategy for the synthesis of other metal oxide embedded structural hybrids and its open up the possibility for the large scale preparation of embedded-rGO NSs hybrids, which may be useful in high-performance energy storage devices.

Acknowledgements

Appendix A. Supplementary data

Supplementary data related to this article can be found at https://doi.org/10.1016/j.electacta.2018.05.157.

References

[1] K.-Y. Oh, B.I. Epureanu, A phenomenological force model of Li-ion battery packs for enhanced performance and health management, J. Power Sources 365 (2017) 220–229.

[2] T. Danner, M. Singh, S. Hein, J. Kaiser, H. Hahn, A. Latz, Thick electrodes for Li-ion batteries: a model based analysis, J. Power Sources 334 (2016) 191–201.

[3] X.-B. Cheng, R. Zhang, C.-Z. Zhao, Q. Zhang, Toward safe lithium metal anode in rechargeable batteries: a review, Chem. Rev. 117 (2017) 10403–10473.

[4] V. Sharova, A. Moretti, T. Diemant, A. Varzi, R.J. Behm, S. Passerini, Comparative study of imide-based Li salts as electrolyte additives for Li-ion batteries, J. Power Sources 375 (2018) 43–52.

[5] L. Yan, J. Yu, H. Luo, Ultrafine TiO$_2$ nanoparticles on reduced graphene oxide as anode materials for lithium ion batteries, Appl. Mater. Today 8 (2017) 31–34.

[6] Y. Wan, Z. Yang, G. Xiong, R. Guo, Z. Liu, H. Luo, Anchoring Fe$_3$O$_4$ nanoparticles on three-dimensional carbon nanofibers toward flexible high-performance anodes for lithium-ion batteries, J. Power Sources 294 (2015) 414–419.

[7] B. Wang, G. Wang, H. Wang, Synthesis and electrochemical investigation of hollow hierarchical metal oxide microspheres for high performance lithium-ion batteries, Electrochim. Acta 156 (2015) 1–10.

[8] L. Yan, Y. Xu, M. Zhou, G. Chen, S. Deng, S. Smirnov, H. Luo, G. Zou, Porous TiO$_2$ conformal coating on carbon nanotubes as energy storage materials, Electrochim. Acta 169 (2015) 73–81.

[9] C.S. Bongu, S. Karuppiah, K. Nallathamby, Validation of green composite containing nanocrystalline Mn$_2$O$_3$ and biocarbon derived from human hair as a potential anode for lithium-ion batteries, J. Mater. Chem. 3 (2015) 23981–23989.

[10] H. Yang, X. Yu, H. Meng, P. Dou, D. Ma, X. Xu, Nanoengineered three-dimensional hybrid Fe$_2$O$_3$@PPy nanotube arrays with enhanced electrochemical performances as lithium–ion anodes, J. Mater. Sci. 50 (2015) 5504–5513.

[11] J.-Y. Shin, J.H. Joo, D. Samuelis, J. Maier, Oxygen-deficient TiO$_{2-\delta}$ nanoparticles via hydrogen reduction for high rate capability lithium batteries, Chem. Mater. 24 (2012) 543–551.

[12] A.S. Arico, P. Bruce, B. Scrosati, J.-M. Tarascon, W. van Schalkwijk, Nanostructured materials for advanced energy conversion and storage devices, Nat. Mater. 4 (2005) 366–377.

[13] M. Armand, J.M. Tarascon, Building better batteries, Nature 451 (2008) 652–657.

[14] J. Ming, J.-B. Park, Y.-K. Sun, Encapsulation of metal oxide nanocrystals into porous carbon with ultrahigh performances in lithium-ion battery, ACS Appl. Mater. Interfaces 5 (2013) 2133–2136.

[15] M.V. Reddy, G.V. Subba Rao, B.V.R. Chowdari, Metal oxides and oxysalts as anode materials for Li ion batteries, Chem. Rev. 113 (2013) 5364–5457.

[16] L. Zhao, M. Gao, W. Yue, Y. Jiang, Y. Wang, Y. Ren, F. Hu, Sandwich-structured Graphene-Fe$_3$O$_4$@Carbon nanocomposites for high-performance lithium-ion batteries, ACS Appl. Mater. Interfaces 7 (2015) 9709–9715.

[17] H. Gwon, J. Hong, H. Kim, D.-H. Seo, S. Jeon, K. Kang, Recent progress on flexible lithium rechargeable batteries, Energy Environ. Sci. 7 (2014) 538–551.

[18] W. Yue, S. Jiang, W. Huang, Z. Gao, J. Li, Y. Ren, X. Zhao, X. Yang, Sandwich-structural graphene-based metal oxides as anode materials for lithium-ion

batteries, J. Mater. Chem. A 1 (2013) 6928–6933.

[19] H. Qiao, L. Xiao, Z. Zheng, H. Liu, F. Jia, L. Zhang, One-pot synthesis of CoO/C hybrid microspheres as anode materials for lithium-ion batteries, J. Power Sources 185 (2008) 486–491.

[20] A.L.M. Reddy, M.M. Shaijumon, S.R. Gowda, P.M. Ajayan, Coaxial MnO$_2$/carbon nanotube array electrodes for high-performance lithium batteries, Nano Lett. 9 (2009) 1002–1006.

[21] J.G. Kim, Y. Kim, Y. Noh, W.B. Kim, Formation of carbon-coated ZnFe$_2$O$_4$ nanowires and their highly reversible lithium storage properties, RSC Adv. 4 (2014) 27714–27721.

[22] J.G. Kim, S.H. Nam, S.H. Lee, S.M. Choi, W.B. Kim, SnO$_2$ nanorod-planted graphite: an effective nanostructure configuration for reversible lithium ion storage, ACS Appl. Mater. Interfaces 3 (2011) 828–835.

[23] F. Jin, Y. Wang, Topotactical conversion of carbon coated Fe-based electrodes on graphene aerogels for lithium ion storage, J. Mater. Chem. A 3 (2015) 14741–14749.

[24] G. Wang, X. Shen, J. Yao, J. Park, Graphene nanosheets for enhanced lithium storage in lithium ion batteries, Carbon 47 (2009) 2049–2053.

[25] K. Chen, S. Song, F. Liu, D. Xue, Structural design of graphene for use in electrochemical energy storage devices, Chem. Soc. Rev. 44 (2015) 6230–6257.

[26] Y. Chen, C. Yan, O.G. Schmidt, Strain-driven formation of multilayer graphene/GeO$_2$ tubular nanostructures as high-capacity and very long-life anodes for lithium-ion batteries, Adv. Energy Mater. 3 (2013) 1269–1274.

[27] W. Wei, S. Yang, H. Zhou, I. Lieberwirth, X. Feng, K. Müllen, 3D graphene foams cross-linked with pre-encapsulated Fe$_3$O$_4$ nanospheres for enhanced lithium storage, Adv. Mater. 25 (2013) 2909–2914.

[28] R. Guo, W. Yue, Y. An, Y. Ren, X. Yan, Graphene-encapsulated porous carbon-ZnO composites as high-performance anode materials for Li-ion batteries, Electrochim. Acta 135 (2014) 161–167.

[29] J. Hassoun, B. Scrosati, Review—advances in anode and electrolyte materials for the progress of lithium-ion and beyond lithium-ion batteries, J. Electrochem. Soc. 162 (2015) A2582–A2588.

[30] C. Uthaisar, V. Barone, Edge effects on the characteristics of Li diffusion in graphene, Nano Lett. 10 (2010) 2838–2842.

[31] K. Persson, V.A. Sethuraman, L.J. Hardwick, Y. Hinuma, Y.S. Meng, A. van der Ven, V. Srinivasan, R. Kostecki, G. Ceder, Lithium diffusion in graphitic carbon, J. Phys. Chem. Lett. 1 (2010) 1176–1180.

[32] S. Yang, G. Cui, S. Pang, Q. Cao, U. Kolb, X. Feng, J. Maier, K. Müllen, Fabrication of cobalt and cobalt oxide/graphene composites: towards high-performance anode materials for lithium ion batteries, ChemSusChem 3 (2010) 236–239.

[33] Z.-S. Wu, W. Ren, L. Wen, L. Gao, J. Zhao, Z. Chen, G. Zhou, F. Li, H.-M. Cheng, Graphene anchored with Co$_3$O$_4$ nanoparticles as anode of lithium ion batteries with enhanced reversible capacity and cyclic performance, ACS Nano 4 (2010) 3187–3194.

[34] E. Samuel, J.-G. Lee, B. Joshi, T.-G. Kim, M.-W. Kim, I.W. Seong, W.Y. Yoon, S.S. Yoon, Supersonic cold spraying of titania nanoparticles on reduced graphene oxide for lithium ion battery anodes, J. Alloys Compd. 715 (2017) 161–169.

[35] Y. Cao, D. Chai, Z. Luo, M. Jiang, W. Xu, C. Xiong, S. Li, H. Liu, D. Fang, Lithium vanadate nanowires@reduced graphene oxide nanocomposites on titanium foil with super high capacities for lithium-ion batteries, J. Colloid Interface Sci. 498 (2017) 210–216.

[36] W.L. Wang, J. Jang, V.H. Nguyen, F.M. Auxilia, H. Song, K. Jang, E.M. Jin, G.-Y. Lee, H.-B. Gu, M.-H. Ham, Cerium vanadate and reduced graphene oxide composites for lithium-ion batteries, J. Alloys Compd. 724 (2017) 1075–1082.

[37] D.S. Shin, H.G. Kim, H.S. Ahn, H.Y. Jeong, Y.-J. Kim, D. Odkhuu, N. Tsogbadrakh, H.-B.-R. Lee, B.H. Kim, Distribution of oxygen functional groups of graphene oxide obtained from low-temperature atomic layer deposition of titanium oxide, RSC Adv. 7 (2017) 13979–13984.

[38] X. Wang, J. Qiu, J. Qu, Z. Wang, D. Su, Fabrication, magnetic properties and self-assembly of hierarchical crystalline hexapod magnetites, RSC Adv. 2 (2012) 4329–4334.

[39] B. Liu, N. Zhong, C. Fan, Y. Zhou, Y. Fan, S. Yu, F. Zhang, L. Dong, Y. Yin, Low temperature synthesis and formation mechanism of carbon encapsulated nanocrystals by electrophilic oxidation of ferrocene, Carbon 68 (2014) 573–582.

[40] J. Wang, M. Gao, H. Pan, Y. Liu, Z. Zhang, J. Li, Q. Su, G. Du, M. Zhu, L. Ouyang, C. Shang, Z. Guo, Mesoporous Fe$_2$O$_3$ flakes of high aspect ratio encased within thin carbon skeleton for superior lithium-ion battery anodes, J. Mater. Chem. A 3 (2015) 14178–14187.

[41] M. Ren, M. Yang, W. Liu, M. Li, L. Su, C. Qiao, X. Wu, H. Ma, Ultra-small Fe$_3$O$_4$ nanocrystals decorated on 2D graphene nanosheets with excellent cycling stability as anode materials for lithium ion batteries, Electrochim. Acta 194 (2016) 219–227.

[42] K. Zhu, Y. Zhang, H. Qiu, Y. Meng, Y. Gao, X. Meng, Z. Gao, G. Chen, Y. Wei, Hierarchical Fe$_3$O$_4$ microsphere/reduced graphene oxide composites as a capable anode for lithium-ion batteries with remarkable cycling performance, J. Alloys Compd. 675 (2016) 399–406.

[43] C. Ma, J. Shi, Y. Zhao, N.-J. Song, Y. Wang, A novel porous reduced micro-crystalline graphene oxide supported Fe$_3$O$_4$@C nanoparticle composite as anode material with excellent lithium storage performances, Chem. Eng. J. 326 (2017) 507–517.

[44] S. Petnikota, H. Maseed, V.V.S.S. Srikanth, M.V. Reddy, S. Adams, M. Srinivasan, B.V.R. Chowdari, Experimental elucidation of a graphenothermal reduction mechanism of Fe$_2$O$_3$: an enhanced anodic behavior of an exfoliated reduced graphene Oxide/Fe$_3$O$_4$ composite in Li-Ion batteries, J. Phys. Chem. C 121 (2017) 3778–3789.

[45] S. Bhuvaneswari, P.M. Pratheeksha, S. Anandan, D. Rangappa, R. Gopalan, T.N. Rao, Efficient reduced graphene oxide grafted porous Fe$_3$O$_4$ composite as a high performance anode material for Li-ion batteries, Phys. Chem. Chem. Phys. 16 (2014) 5284–5294.

[46] R. Kumar, R.K. Singh, P.K. Dubey, D.P. Singh, R.M. Yadav, Self-assembled hierarchical formation of conjugated 3D cobalt oxide nanobead–CNT–graphene nanostructure using microwaves for high-performance supercapacitor electrode, ACS Appl. Mater. Interfaces 7 (2015) 15042–15051.

[47] R. Kumar, H.-J. Kim, S. Park, A. Srivastava, I.-K. Oh, Graphene-wrapped and cobalt oxide-intercalated hybrid for extremely durable super-capacitor with ultrahigh energy and power densities, Carbon 79 (2014) 192–202.

[48] L. Staudenmaier, Verfahren zur Darstellung der Graphitsäure, Ber. Dtsch. Chem. Ges. 31 (1898) 1481–1487.

[49] R. Kumar, E.T.S.G. da Silva, R.K. Singh, R. Savu, A.V. Alaferdov, L.C. Fonseca, L.C. Carossi, A. Singh, S. Khandka, K.K. Kar, O.L. Alves, L.T. Kubota, S.A. Moshkalev, Microwave-assisted synthesis of palladium nanoparticles intercalated nitrogen doped reduced graphene oxide and their electrocatalytic activity for direct-ethanol fuel cells, J. Colloid Interface Sci. 515 (2018) 160–171.

[50] R. Kumar, R.K. Singh, D.P. Singh, R. Savu, S.A. Moshkalev, Microwave heating time dependent synthesis of various dimensional graphene oxide supported hierarchical ZnO nanostructures and its photoluminescence studies, Mater. Des. 111 (2016) 291–300.

[51] R. Kumar, R.K. Singh, A.R. Vaz, R. Savu, S.A. Moshkalev, Self-assembled and one-step synthesis of interconnected 3D network of Fe$_3$O$_4$/Reduced graphene oxide nanosheets hybrid for high-performance supercapacitor electrode, ACS Appl. Mater. Interfaces 9 (2017) 8880–8890.

[52] R. Kumar, P.K. Dubey, R.K. Singh, A.R. Vaz, S.A. Moshkalev, Catalyst-free synthesis of a three-dimensional nanoworm-like gallium oxide-graphene nanosheet hybrid structure with enhanced optical properties, RSC Adv. 6 (2016) 17669–17677.

[53] R. Kumar, R.K. Singh, R. Savu, P.K. Dubey, P. Kumar, S.A. Moshkalev, Microwave-assisted synthesis of void-induced graphene-wrapped nickel oxide hybrids for supercapacitor applications, RSC Adv. 6 (2016) 26612–26620.

[54] J. Su, M. Cao, L. Ren, C. Hu, Fe$_3$O$_4$–Graphene nanocomposites with improved lithium storage and magnetism properties, J. Phys. Chem. C 115 (2011) 14469–14477.

[55] Q. Han, Z. Wang, J. Xia, S. Chen, X. Zhang, M. Ding, Facile and tunable fabrication of Fe$_3$O$_4$/graphene oxide nanocomposites and their application in the magnetic solid-phase extraction of polycyclic aromatic hydrocarbons from environmental water samples, Talanta 101 (2012) 388–395.

[56] C. Liang, S. Huang, W. Zhao, W. Liu, J. Chen, H. Liu, Y. Tong, Polyhedral Fe$_3$O$_4$ nanoparticles for lithium ion storage, N. J. Chem. 39 (2015) 2651–2656.

[57] K.N. Kudin, B. Ozbas, H.C. Schniepp, R.K. Prud'homme, I.A. Aksay, R. Car, Raman spectra of graphite oxide and functionalized graphene sheets, Nano Lett. 8 (2008) 36–41.

[58] B. Shen, W. Zhai, M. Tao, J. Ling, W. Zheng, Lightweight, multifunctional polyetherimide/graphene@Fe$_3$O$_4$ composite foams for shielding of electromagnetic pollution, ACS Appl. Mater. Interfaces 5 (2013) 11383–11391.

[59] C. Yang, Y. Qing, K. An, Z. Zhang, L. Wang, C. Liu, Facile synthesis of the N-doped graphene/nickel oxide with enhanced electrochemical performance for rechargeable lithium-ion batteries, Mater. Chem. Phys. 195 (2017) 149–156.

[60] N. Hong, L. Song, T.R. Hull, A.A. Stec, B. Wang, Y. Pan, Y. Hu, Facile preparation of graphene supported Co$_3$O$_4$ and NiO for reducing fire hazards of polyamide 6 composites, Mater. Chem. Phys. 142 (2013) 531–538.

[61] A. Al-Nafiey, A. Kumar, M. Kumar, A. Addad, B. Sieber, S. Szunerits, R. Boukherroub, S.L. Jain, Nickel oxide nanoparticles grafted on reduced graphene oxide (rGO/NiO) as efficient photocatalyst for reduction of nitro-aromatics under visible light irradiation, J. Photochem. Photobiol. A Chem. 336 (2017) 198–207.

[62] L. Wang, Y. Huang, C. Li, J. Chen, X. Sun, Enhanced microwave absorption properties of N-doped graphene@PANI nanorod arrays hierarchical structures modified by Fe3O4 nanoclusters, Synth. Met. 198 (2014) 300–307.

[63] B. Qu, C. Zhu, C. Li, X. Zhang, Y. Chen, Coupling hollow Fe$_3$O$_4$–Fe nanoparticles with graphene sheets for high-performance electromagnetic wave absorbing material, ACS Appl. Mater. Interfaces 8 (2016) 3730–3735.

[64] T. Wang, L. Zhang, H. Wang, W. Yang, Y. Fu, W. Zhou, W. Yu, K. Xiang, Z. Su, S. Dai, L. Chai, Controllable synthesis of hierarchical porous Fe$_3$O$_4$ particles mediated by poly(diallyldimethylammonium chloride) and their application in arsenic removal, ACS Appl. Mater. Interfaces 5 (2013) 12449–12459.

[65] M. Zong, Y. Huang, Y. Zhao, X. Sun, C. Qu, D. Luo, J. Zheng, Facile preparation, high microwave absorption and microwave absorbing mechanism of RGO-Fe$_3$O$_4$ composites, RSC Adv. 3 (2013) 23638–23648.

[66] J. Luo, J. Liu, Z. Zeng, C.F. Ng, L. Ma, H. Zhang, J. Lin, Z. Shen, H.J. Fan, Three-dimensional graphene foam supported Fe$_3$O$_4$ lithium battery anodes with long cycle life and high rate capability, Nano Lett. 13 (2013) 6136–6143.

[67] M. Chen, C. Hou, D. Huo, H. Fa, Y. Zhao, C. Shen, A sensitive electrochemical DNA biosensor based on three-dimensional nitrogen-doped graphene and Fe$_3$O$_4$ nanoparticles, Sens. Actuators B Chem. 239 (2017) 421–429.

[68] T. Fujii, F.M.F. de Groot, G.A. Sawatzky, F.C. Voogt, T. Hibma, K. Okada, In situ XPS analysis of various iron oxide films grown by NO$_2$-assisted molecular-beam epitaxy, Phys. Rev. B 59 (1999) 3195–3202.

[69] X. Yi, W. He, X. Zhang, Y. Yue, G. Yang, Z. Wang, M. Zhou, L. Wang, Graphene-like carbon sheet/Fe_3O_4 nanocomposites derived from soda papermaking black liquor for high performance lithium ion batteries, Electrochim. Acta 232 (2017) 550—560.

[70] D. Chen, G. Ji, Y. Ma, J.Y. Lee, J. Lu, Graphene-encapsulated hollow Fe_3O_4 nanoparticle aggregates as a high-performance anode material for lithium ion batteries, ACS Appl. Mater. Interfaces 3 (2011) 3078—3083.

[71] B. Jin, G. Chen, X. Zhong, Y. Liu, K. Zhou, P. Sun, P. Lu, W. Zhang, J. Liang, Graphene/Fe_3O_4 hollow sphere nanocomposites as superior anode material for lithium ion batteries, Ceram. Int. 40 (2014) 10359—10365.

[72] J. Zhao, S. Zhang, W. Liu, Z. Du, H. Fang, Fe_3O_4/PPy composite nanospheres as anode for lithium-ion batteries with superior cycling performance, Electrochim. Acta 121 (2014) 428—433.

[73] X. Hu, M. Ma, M. Zeng, Y. Sun, L. Chen, Y. Xue, T. Zhang, X. Ai, R.G. Mendes, M.H. Rümmeli, L. Fu, Supercritical carbon dioxide anchored Fe_3O_4 nanoparticles on graphene foam and lithium battery performance, ACS Appl. Mater. Interfaces 6 (2014) 22527—22533.

[74] Y. Qi, H. Zhang, N. Du, D. Yang, Highly loaded CoO/graphene nanocomposites as lithium-ion anodes with superior reversible capacity, J. Mater. Chem. A 1 (2013) 2337—2342.

[75] G. Zhou, D.-W. Wang, F. Li, L. Zhang, N. Li, Z.-S. Wu, L. Wen, G.Q. Lu, H.-M. Cheng, Graphene-Wrapped Fe_3O_4 anode material with improved reversible capacity and cyclic stability for lithium ion batteries, Chem. Mater. 22 (2010) 5306—5313.

[76] W.-M. Zhang, X.-L. Wu, J.-S. Hu, Y.-G. Guo, L.-J. Wan, Carbon coated Fe_3O_4 nanospindles as a superior anode material for lithium-ion batteries, Adv. Funct. Mater. 18 (2008) 3941—3946.

[77] P.L. Taberna, S. Mitra, P. Poizot, P. Simon, J.M. Tarascon, High rate capabilities Fe_3O_4-based Cu nano-architectured electrodes for lithium-ion battery applications, Nat. Mater. 5 (2006) 567—573.

[78] J. Zhao, B. Yang, Z. Zheng, J. Yang, Z. Yang, P. Zhang, W. Ren, X. Yan, Facile preparation of one-dimensional wrapping structure: graphene nanoscroll-wrapped of Fe_3O_4 nanoparticles and its application for lithium-ion battery, ACS Appl. Mater. Interfaces 6 (2014) 9890—9896.

[79] S.K. Behera, Enhanced rate performance and cyclic stability of Fe_3O_4-graphene nanocomposites for Li ion battery anodes, Chem. Commun. 47 (2011) 10371—10373.

[80] Y. Dong, Z. Zhang, Y. Xia, Y.-S. Chui, J.-M. Lee, J.A. Zapien, Green and facile synthesis of Fe_3O_4 and graphene nanocomposites with enhanced rate capability and cycling stability for lithium ion batteries, J. Mater. Chem. A 3 (2015) 16206—16212.

[81] Y. Dong, R. Ma, M. Hu, H. Cheng, Q. Yang, Y.Y. Li, J.A. Zapien, Thermal evaporation-induced anhydrous synthesis of Fe_3O_4-graphene composite with enhanced rate performance and cyclic stability for lithium ion batteries, Phys. Chem. Chem. Phys. 15 (2013) 7174—7181.

[82] P. Lian, X. Zhu, H. Xiang, Z. Li, W. Yang, H. Wang, Enhanced cycling performance of Fe_3O_4—graphene nanocomposite as an anode material for lithium-ion batteries, Electrochim. Acta 56 (2010) 834—840.

[83] J.Z. Wang, C. Zhong, D. Wexler, N.H. Idris, Z.X. Wang, L.Q. Chen, H.K. Liu, Graphene-encapsulated Fe_3O_4 nanoparticles with 3D laminated structure as superior anode in lithium ion batteries, Chem. A Eur. J. 17 (2011) 661—667.

[84] X. Li, X. Huang, D. Liu, X. Wang, S. Song, L. Zhou, H. Zhang, Synthesis of 3D hierarchical Fe_3O_4/Graphene composites with high lithium storage capacity and for controlled drug delivery, J. Phys. Chem. C 115 (2011) 21567—21573.

[85] X. Huang, X. Zhou, K. Qian, D. Zhao, Z. Liu, C. Yu, A magnetite nanocrystal/graphene composite as high performance anode for lithium-ion batteries, J. Alloys Compd. 514 (2012) 76—80.

[86] Y. Chen, B. Song, L. Lu, J. Xue, Ultra-small Fe_3O_4 nanoparticle decorated graphene nanosheets with superior cyclic performance and rate capability, Nanoscale 5 (2013) 6797—6803.

[87] M. Sathish, T. Tomai, I. Honma, Graphene anchored with Fe_3O_4 nanoparticles as anode for enhanced Li-ion storage, J. Power Sources 217 (2012) 85—91.

[88] C.-T. Hsieh, J.-Y. Lin, C.-Y. Mo, Improved storage capacity and rate capability of Fe_3O_4—graphene anodes for lithium-ion batteries, Electrochim. Acta 58 (2011) 119—124.

[89] L. Li, A. Kovalchuk, H. Fei, Z. Peng, Y. Li, N.D. Kim, C. Xiang, Y. Yang, G. Ruan, J.M. Tour, Enhanced cycling stability of lithium-ion batteries using graphene-wrapped Fe_3O_4-Graphene nanoribbons as anode materials, Adv. Energy Mater. 5 (2015), 1500171.

[90] W. Wei, S. Yang, H. Zhou, I. Lieberwirth, X. Feng, K. Müllen, 3D graphene foams cross-linked with pre-encapsulated Fe_3O_4 nanospheres for enhanced lithium storage, Adv. Mater. 25 (2013) 2909—2914.

[91] L. Ji, Z. Tan, T.R. Kuykendall, S. Aloni, S. Xun, E. Lin, V. Battaglia, Y. Zhang, Fe_3O_4 nanoparticle-integrated graphene sheets for high-performance half and full lithium ion cells, Phys. Chem. Chem. Phys. 13 (2011) 7170—7177.

[92] R. Kumar, E. Joanni, R.K. Singh, E.T.S.G. da Silva, R. Savu, L.T. Kubota, S.A. Moshkalev, Direct laser writing of micro-supercapacitors on thick graphite oxide films and their electrochemical properties in different liquid inorganic electrolytes, J. Colloid Interface Sci. 507 (2017) 271—278.

[93] W. Lei, Y. Liu, X. Si, J. Xu, W. Du, J. Yang, T. Zhou, J. Lin, Synthesis and magnetic properties of octahedral Fe_3O_4 via a one-pot hydrothermal route, Phys. Lett. A 381 (2017) 314—318.

[94] A. Mitra, J. Mohapatra, S.S. Meena, C.V. Tomy, M. Aslam, Verwey transition in ultrasmall-sized octahedral Fe_3O_4 nanoparticles, J. Phys. Chem. C 118 (2014) 19356—19362.

[95] Z.L. Wang, Transmission electron microscopy of shape-controlled nanocrystals and their assemblies, J. Phys. Chem. B 104 (2000) 1153—1175.

[96] B.Y. Geng, J.Z. Ma, J.H. You, Controllable synthesis of single-crystalline Fe_3O_4 polyhedra possessing the active basal facets, Cryst. Growth Des. 8 (2008) 1443—1447.

[97] H. Deng, X. Li, Q. Peng, X. Wang, J. Chen, Y. Li, Monodisperse magnetic single-crystal ferrite microspheres, Angew. Chem. Int. Ed. 44 (2005) 2782—2785.